10-1996

Modeling Nutrient and Plankton Processes in the California Coastal Transition Zone: 2. A Three-Dimensional Physical-Bio-Optical Model

J. R. Moisan

Eileen E. Hofmann
Old Dominion University, ehofmann@odu.edu

D. B. Haidvogel

Original Publication Citation

Moisan, J.R., Hofmann, E.E., & Haidvogel, D.B. (1996). Modeling nutrient and plankton processes in the California coastal transition zone: 2. A three-dimensional physical-bio-optical model. *Journal of Geophysical Research, 101*(C10), 22677-22691. doi: 10.1029/96JC01719

JOURNAL OF GEOPHYSICAL RESEARCH, VOL. 101, NO. C10, PAGES 22,677–22,691, OCTOBER 15, 1996

Modeling nutrient and plankton processes in the California coastal transition zone 2. A three-dimensional physical-bio-optical model

J. R. Moisan[1] and E. E. Hofmann
Center for Coastal Physical Oceanography, Department of Oceanography
Old Dominion University, Norfolk, Virginia

D. B. Haidvogel
Institute of Marine and Coastal Sciences, Rutgers University, New Brunswick, New Jersey

Abstract. A three-dimensional (3-D) primitive equation model, developed to simulate the circulation features (filaments) observed in the California coastal transition zone (CTZ), was coupled to a nine-component food web model and a bio-optical model. The simulated flow fields from a 3-D primitive equation model are used to advect the constituents of the food web model, which include silicate, nitrate, ammonium, two phytoplankton size fractions, copepods, doliolids, euphausiids, and a detritus pool. The bio-optical model simulates the wavelength-dependent attenuation of the subsurface irradiance field. The overall objective of this modeling study was to understand and quantify the processes that contribute to the spatial and temporal development of nutrient and plankton distributions in the CTZ. The resulting simulated 3-D nutrient, plankton and submarine light fields agree well with those observed within the CTZ. Specifically, high nutrient and plankton biomass occur onshore and within the core of the simulated filament. Variations in the depth of the 1% light level, which result from the simulated plankton distributions, shallows to less than 30 m in regions of high phytoplankton biomass, and deepens to greater than 75 m in regions of low phytoplankton biomass. The onshore and offshore surface carbon flux patterns are similar in shape due to the meander-like flow patterns of the filament; however, the net across-shore area-integrated carbon flux is predominantly offshore. The total 20-day integrated carbon transport for the model domain varies with distance from shore and is highest (35 x 10^9 g C) in the region where the filament circulation pattern develops into an anticyclonic and cyclonic pair of eddies. The annual integrated carbon transport by filaments along the California coast is estimated to be 1.89 x 10^{12} g C.

1. Introduction

During the past decade, increased awareness and concern for the California coastal regions has resulted in a number of research programs (Table 1) that had as their primary focus the understanding of oceanographic processes within the California coastal ocean. An objective that was common to all these programs was the understanding of across-shore transfer of mass and energy within coastal regions. One of these programs was the Coastal Transition Zone (CTZ) study [*Brink and Cowles,* 1991; *Strub et al.,* 1991], which took place from 1986 to 1988 and focused on a region off the coast of California (Figure 1). This program had as a primary objective the understanding of the physical and biological nature, structure and cause of formation of cold filaments [*Coastal Transition Zone Group,* 1988], which were often observed in satellite sea surface temperature and pigment concentration images of the waters off the western coast of North America [*Brink and Cowles,* 1991]. The CTZ program consisted of two field sampling seasons (1987 and 1988), the data from which have provided the basis for this study.

Previous studies of the region off California (Table 1) show that it is primarily a coastal upwelling ecosystem. During spring and summer months, upwelling favorable winds from the north cause a surface divergence at the coast which injects nutrient-rich waters from depth into the euphotic zone. This seasonal pulse of nutrients supports coastal phytoplankton blooms which are

[1]Now at Physical Oceanography Research Division, Scripps Institution of Oceanography, La Jolla, California.

Paper number 96JC01719.
0148-0227/96/96JC-01719$09.00

Table 1. Oceanographic Programs Along the California Coast

Program Name	Sampling Dates	Region	Reference
California Cooperative Oceanic Fisheries Investigations (CalCOFI)	1949–Present	24°–38°N	*Chelton* [1984]
Coastal Ocean Dynamics Experiment (CODE 1 and 2)	1981–1982	38°–39°N	*Beardsley and Lentz* [1987]
Ocean Prediction Through Observations, Modeling, and Analysis (OPTOMA 21 and 22)	1982	37°–40°N	*Mooers and Robinson* [1984]
Organization of Persistent Upwelling Features (OPUS)	1983	34°–35°N	*Atkinson et al.* [1986]
Central California Coastal Circulation Study (CCCCS)	1984–1985	34°–38°N	*Chelton et al.* [1988]
Coastal Transition Zone (CTZ)	1987–1988	37°–42°N	*Brink and Cowles* [1991]
Northern California Coastal Circulation Study (NCCCS)	1987–1989	38°–42°N	*Magnell et al.* [1990]

dominated by silicate-dependent diatoms and nitrate-dependent dinoflagellates. The phytoplankton bloom in turn supports a suite of secondary producers such as copepods, euphausiids, and doliolids. In general, the productivity of coastal waters decreases offshore of the coastal upwelling region [*Smith et al.*, 1988; *Hood et al.*, 1990]. Superimposed on the coastal upwelling circulation are the processes and dynamics associated with the meridional flows of the California Current system (CCS) and the filaments associated with the CTZ.

Satellite-derived observations of the ocean surface temperature (advanced very high resolution radiometer, AVHRR) or pigment (coastal zone color scanner, CZCS) distributions in the CCS show the presence of filament-like structures propagating offshore during periods of intense coastal upwelling (most active in the spring and summer months) [*Bernstein et al.*, 1977; *Traganza et al.*, 1980, 1981; *Brink and Cowles*, 1991; *Breaker and Gilliland*, 1981; *Abbott and Zion*, 1985, 1987; *Stramma et al.*, 1986; *Thomson and Papadakis*, 1987]. *Strub et al.* [1991] outlined three conceptual models to explain the mesoscale current structure observed in the CTZ. The first model suggests that the filaments in the CTZ are the result of offshore flowing jets (squirts) which advect cold, upwelled coastal water offshore. At the offshore extent of this feature are two counter rotating eddies. This model is supported by the observation of mesoscale eddy dipoles in the offshore California Current [*Simpson and Lynn*, 1990]. The second conceptual model envisions the CTZ as a mesoscale eddy field embedded within the slow, southward flowing CCS. This conceptual model is supported by the observation of eddies within the CCS, which give rise to squirt-like features as they draw recently upwelled waters offshore [*Mooers and Robinson*, 1984; *Rienecker et al.*, 1987], and by the observation of an offshore mesoscale eddy field in the California Current region [*White et al.*, 1990]. The third conceptual model, the meandering jet theory, is strongly supported by observations obtained during the CTZ field and modeling experiments [*Strub et al.*, 1991]. This model suggests that most of the offshore transport in the CCS occurs as a meandering jet which transports nutrient-poor waters into the CTZ from the north. In conjunction with this meandering jet, strong cutoff eddies and squirts are observed to form. Cold, upwelled, nutrient-rich water lying between this meandering jet and the coast is then advected offshore. What model type the filaments fall under greatly affects the way in which mass, energy, biology, and nutrients along the coast are transported into the offshore regions.

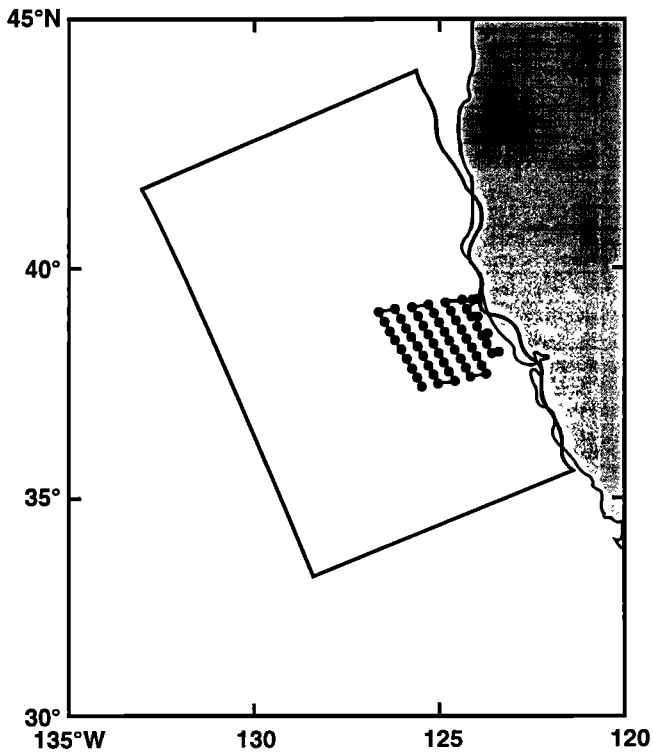

Figure 1. The Coastal Transition Zone study region. The region included in the CTZ physical-bio-optical model domain is indicated by the box. Within this domain, the standardized station grid, which was used during the 1988 CTZ surveys, is shown. The black dots indicate the station locations.

Other studies have investigated the time and space variability of the plankton and nutrient fields associated with the CCS and CTZ. On a regional scale, the biological and chemical distributions within the CCS are greatly influenced by the strong seasonal variation in the coastal wind field. In the spring, the coastal wind

field changes to upwelling favorable in a short period of time [*Lentz,* 1987]. The effect of the seasonal change in wind field pattern on the phytoplankton populations has been the subject of numerous studies [*Abbott and Zion,* 1987; *Michaelsen et al.,* 1988; *Abbott and Barksdale,* 1991; *Thomas and Strub,* 1989, 1990]. During the spring transition, pigment concentrations along the coast increase from 0.5 mg chlorophyll *a* m^{-3} to greater than 3 mg chlorophyll *a* m^{-3} [*Thomas and Strub,* 1989]. The spatial and temporal variability of the phytoplankton populations in this region has been attributed to large- and small-scale variations in the wind stress and wind stress curl [*Abbott and Zion,* 1987; *Abbott and Barksdale,* 1991]. In general, the coastal upwelling zone consists of an inshore region which contains high phytoplankton populations in conjunction with high nutrient concentrations. Offshore, the phytoplankton and nutrient concentrations decrease and become increasingly variable [*Abbott and Zion,* 1987].

The effect of the filaments is to entrain the recently upwelled waters and transport them offshore within the filament. However, given the complex, 3-D and time-dependent nature of these filaments, understanding and quantification of across-shore exchange of nutrients and biomass is difficult. The ephemeral nature of the filaments that occur in the CTZ makes modeling studies an important part of understanding the physical and biological interactions that are responsible for the plankton dynamics associated with the filaments.

This paper, the second in a series of three papers [*Moisan and Hofmann,* this issue(a, b)] presents the results from a 3-D, time-dependent, physical-bio-optical model. The model is a nine-component food web model which has been coupled to a wavelength-dependent subsurface irradiance model and a 3-D, primitive equation, regional circulation model. This model was developed for the CTZ with the overall objective of quantifying and understanding the physical and biological processes associated with the across-shore transport of nutrients and biomass. The results from this model are compared with data collected during the CTZ field surveys. While this study was specific to the CTZ, the model and approaches used are appropriate for addressing similar questions in other coastal environments.

The primary objective of this paper is to simulate the plankton dynamics within the CTZ during a period in time that a filament forms and extends offshore. The resulting simulation is then used to determine the importance of various processes, such as advection, in situ growth, and grazing, in the transport of particulate organic carbon across-shore. The second objective is to determine the flux and total transport of this carbon and their relation to the biomass and across-shore velocity fields. The resulting across-shore carbon flux estimates are compared to carbon flux measurements calculated from data obtained during the CTZ field surveys.

The second section presents the model equations and the initial conditions used for the model simulation. The resulting physical, bio-optical, and across-shore carbon flux fields are presented in section 3. Finally, section 4 presents a discussion of the results.

2. Methods

2.1. Model Equations

The model is a 3-D, time-dependent, physical-bio-optical model. The physical portion includes the effects of vertical (biological and physical) and horizontal (physics only) velocity and vertical and horizontal diffusion. The bio-optical portion of the model consists of the nine-component food web and bio-optical model presented by *Moisan and Hofmann* [this issue(a)]. The biological portion of the model therefore is a system of nine coupled partial differential equations that govern the spatial and temporal distribution of a nonconservative quantity, which is of the form

$$\frac{\partial B}{\partial t} = \nabla \cdot K \nabla B - (\vec{v} + \vec{v}_{\text{biology}}) \cdot \nabla B + S - r_{\text{nudge}}(B - B_{\text{clim}}) \quad (1)$$

where B is a nonconservative quantity (one of the nine components in the biological model), $\vec{v}$ is the vertical and horizontal velocity of the fluid, $\vec{v}_{\text{biology}}$ is the vertical sinking rate of the biological components. The vertical sinking rates for the large (LPP, 1 m d^{-1}) and small (SPP, 0.1 m d^{-1}) phytoplankton size fractions were estimated from *Beinfang and Szyper* [1982] and *Smayda* [1970]. Because no vertical migration was observed to occur in the CTZ, the zooplankton portion of the model was not given any vertical migration behavior [*Huntley et al.,* 1995]. The velocity, $\vec{v}$, and the kinematic eddy diffusivity, K, were obtained as described below. The source or sink term, S, for biological component is previously defined by *Moisan and Hofmann* [this issue(a)], and r_{nudge} is the rate at which the biological component is nudged back to the climatological mean of the biological component, B_{clim}.

2.2. Velocity and Diffusion

The velocities, $\vec{v}$, and kinematic eddy diffusivities, K, which were used to advect and diffuse the biological distributions, were provided by the simulated circulation distributions obtained simultaneously from the regional primitive equation model that was developed for the CTZ region [*Haidvogel et al.,* 1991a]. Because of this, the physical-bio-optical model uses a domain (Figure 1) and grid (Figure 2) that are identical to those used for the regional circulation model. The physical dynamics that are included in the circulation model and the numerical solution techniques are presented by *Haidvogel et al.* [1991a, b] and *Hedström* [1990]. The governing equations which are used in this model are the hydrostatic primitive equations:

$$\frac{\partial u}{\partial t} + \vec{v} \cdot \nabla u - fv = -\frac{\partial \phi}{\partial x} + \mathcal{F}_u + \mathcal{D}_u \quad (2)$$

$$\frac{\partial v}{\partial t} + \vec{v} \cdot \nabla v + fu = -\frac{\partial \phi}{\partial y} + \mathcal{F}_v + \mathcal{D}_v \quad (3)$$

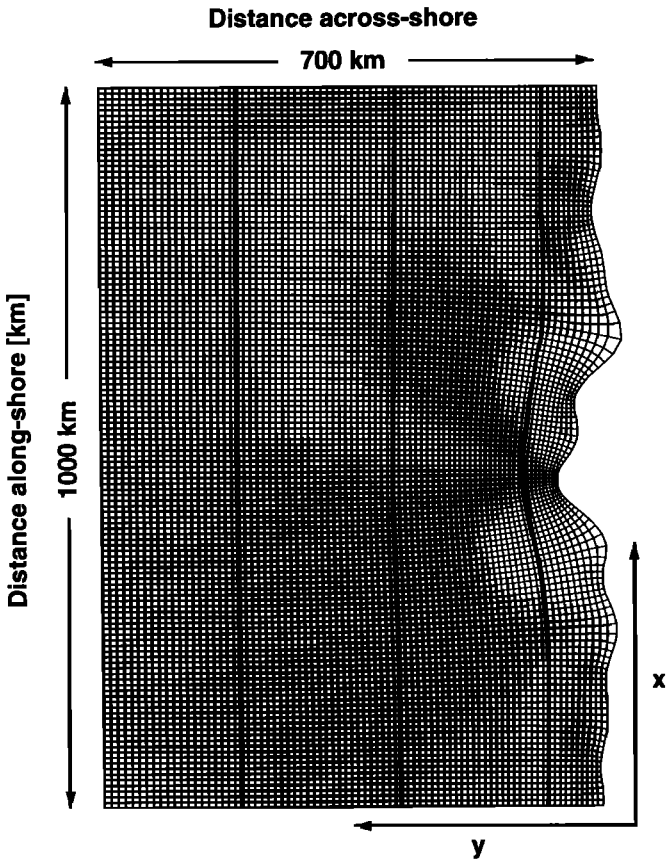

Figure 2. The orthogonal curvilinear grid (129 x 81 points) used for the 3-D numerical model. The domain is 1000 km wide (along-shelf) and 700 km wide (across-shore). The three solid wide lines indicate along-shelf sections that are extracted from the model to display selected vertical distributions.

$$\frac{\partial T}{\partial t} + \vec{v} \cdot \nabla T = \mathcal{F}_T + \mathcal{D}_T \quad (4)$$

$$\frac{\partial S}{\partial t} + \vec{v} \cdot \nabla S = \mathcal{F}_S + \mathcal{D}_S \quad (5)$$

$$\frac{\partial \phi}{\partial z} = -\frac{\rho g}{\rho_0} \quad (6)$$

$$\frac{\partial u}{\partial x} + \frac{\partial v}{\partial y} + \frac{\partial w}{\partial z} = 0. \quad (7)$$

The terms and parameters in equations (2)-(7) are defined in Table 2. Equations (2) and (3) express the zonal and meridional momentum balances, respectively. The time evolution of the perturbation temperature, $T(x, y, z, t)$, and salinity, $S(x, y, z, t)$, fields, which govern the perturbation density, $\rho(x, y, z, t)$, are given by equations (4) and (5), respectively. The vertical momentum balance, equation (6), is obtained by using the Boussinesq approximation, where density variations are neglected in the momentum equations except for their contribution to the buoyancy forcing. Finally, equation (7) is the continuity equation for an incompressible fluid. Further descriptions of these equations and their terms are presented by *Hedström* [1990].

2.3. Biological Components and Optics

The subsurface irradiance field and the phytoplankton, zooplankton, and nutrient source and sink terms in the 3-D model were calculated using the same formulations developed for the one-dimensional model [*Moisan and Hofmann,* this issue(a)]. However, these formulations were extended to three dimensions by allowing them to occur at all locations in the spatial field.

2.4. Model Implementation and Initial Conditions

The 3-D time-dependent physical-bio-optical model was initialized using the simulated circulation and density fields from day 140 of a circulation calculation done for the CTZ [*Haidvogel et al.,* 1991a] and integrated forward in time for 20 days. This initial condition was chosen because it was during this time period that a filament was observed to form at the coastal bump and propagate offshore. The total integration time of 20 days also coincides with the generation time of a filament [*Kosro and Huyer,* 1986]. Results from the one-dimensional model simulations, which were integrated for 100 days, showed that 20 days was an adequate timescale for the simulations to adjust from the initial conditions [*Moisan and Hofmann,* this issue(a)]. As in the one-dimensional model, a spectral collocation method was used to solve the time- and space-dependent system of equations. This provides consistency with the circulation model. The time stepping techniques are presented by *Hedström* [1990].

All the initial and climatological conditions for the 3-D model were determined from relationships derived from the CTZ field observations [*Strub et al.,* 1991].

Table 2. Definition of Terms in the Hydrostatic Primitive Equations For the 3-D Model

Term	Definition
(u, v, w)	(x, y, z) components of the velocity vector, $\vec{v}$
$\rho_0 + \rho(x, y, z, t)$	total density
$T(x, y, z, t)$	total temperature
$S(x, y, z, t)$	total salinity
$\phi(x, y, z, t)$	dynamic pressure, (ρ/ρ_0)
$f(x, y)$	Coriolis parameter
g	acceleration of gravity
$(\mathcal{F}_u, \mathcal{F}_v, \mathcal{F}_T, \mathcal{F}_S)$	forcing terms
$(\mathcal{D}_u, \mathcal{D}_v, \mathcal{D}_T, \mathcal{D}_S)$	diffusive terms

The salinity and temperature fields were derived using the standard equation of state relationship [*Millero and Poisson,* 1981] and the mean CTZ temperature versus salinity relationship. However, in order to decrease the number of calculations, the salinity field within the physical model was replaced with the actual density values. An example of the initial (model day 140) vertical velocity and density distributions from circulation model is shown in Plate 1a.

Initial distributions for the large and small phytoplankton fractions were obtained using the chlorophyll *a* to percent size fractionation relationship and the chlorophyll *a* to dynamic height ($\phi_{0/500}$ m^2 s^{-2}) relationship, both from *Chavez et al.* [1991]. Initial distributions for the copepod, euphausiid, and doliolid fields were calculated from individual copepod, euphausiid, and doliolid biomass to dynamic height relationships obtained from observations from the CTZ [*Mackas et al.,* 1991]. The initial nitrate and silicate fields were obtained using the initial temperature field with the nutrient to temperature relationships obtained for the CTZ [*Huyer et al.,* 1991]. The initial ammonium and detritus fields were set to a constant value of zero.

The initial conditions for the phytoplankton, zooplankton, and detritus varied with horizontal position but not with depth. Results from the 1-D model presented by *Moisan and Hofmann* [this issue(a)] demonstrated that the bio-optical model is capable of creating depth-dependent structures within 3 days of simulation. Initializing the model domain with no vertical dependence allowed the model to develop its own vertical structures. Also, we were unable to draw any general vertical relationships from the CTZ field survey data.

The climatological fields for nitrate and silicate were calculated using the same method as that used to calculate the initial conditions except that the 3-D climatological temperature field used in the circulation model was used instead of the temperature field derived from day 140. The climatological ammonium, detritus, phytoplankton, and zooplankton fields were set to zero. By setting the climatologies of the biological fields to zero, the resulting biological fields are then a result of the biological forcing and not a result of the climatological forcing.

3. Results

3.1. Simulated Circulation Fields

The 3-D model simulations used 20 days of simulated circulation fields that were obtained after 140 days of integration. This time corresponds to a point in the circulation simulation when a filament was observed to form and develop offshore [*Haidvogel et al.,* 1991a]. The large-scale horizontal structure of the simulated flow field from day 140 (Plate 1a), which is the initial velocity field used for the simulations, shows primarily southward flow along the coastal boundary that is associated with the California Current. Average southward velocities are of the order of 45 cm s^{-1}. Near the center of the model region, an offshore-extending filament has formed in the vicinity of a coastal bump. Flow is offshore on the northern side and onshore on the southern side of the filament, with velocities of about 50 cm s^{-1} on both sides. The narrow feature located north and offshore of the filament is the decaying remnant of a previously formed filament.

The vertical flow patterns show small-scale regions of upwelling and downwelling along the coastal shelf region and somewhat larger regions of upwelling and downwelling along the coast and near the shelf break which is about 50–100 km offshore. These features have been attributed to small-scale frontal instabilities and possibly coastal trapped waves [*Haidvogel et al.,* 1991a]. Vertical velocities in the offshore extending filament indicate downwelling and upwelling in the north and south sides of the feature, respectively. Maximum upwelling velocities are on the order of 10–20 m d^{-1}.

Ten days later (Plate 1b), the filament has elongated and extends offshore about 430 km. The across-filament width has decreased to about 100 km, and a cyclonic eddy appears to be forming at the outer end of the feature. Strong offshore and onshore velocities are found on the northern and southern sides of the filament, respectively, and maximum velocities within the filament reach 73 cm s^{-1}. The filament has also moved southward by about 70 km relative to its position on day 140.

By day 160 (Plate 1c) the filament extends offshore about 590 km, and a cyclonic eddy is forming at its outer extent. A weaker anticyclonic eddy is forming to the north of the feature and is expressed by the northward deflection of the tip of the filament. Maximum velocities in the filament are about 90 cm s^{-1}.

3.2. Simulated Biological and Optical Distributions

The distribution of the phytoplankton, integrated over the depth of the simulated euphotic zone (1% photosynthetically available radiation, PAR), on day 140 (Plate 2a) shows the highest concentrations ($\approx$ 44 mg N m^{-3}) along the coast and within the filament. The sharp gradient in the integrated phytoplankton field at the coast coincides with the density gradient at this location (Plate 1a). The euphotic zone depth is shallowest ($\approx$ 30 m) along the coastal regions and within the filament, which coincides with the regions of highest chlorophyll concentration. The euphotic zone deepens to about 180 m offshore of the shelf region and outside of the filament. Sharp gradients in the depth of the euphotic zone occur in the coastal region and along the northern and southern sides of the filament.

Over the next 10 days (Plate 2b) the horizontal structure of the phytoplankton evolves similarly to that for the circulation field. Phytoplankton concentrations of 25 mg N m^{-3} now extend about 440 km offshore in the filament. However, the overall phytoplankton concentration in the filament has decreased relative to that at day 140 (Plate 2a). The decrease arises through loss of biomass from the filament by phytoplankton death, zoo-

plankton grazing, cell sinking, and across-filament shear [*Hofmann et al.*, 1991]. The decrease within the filament is consistent with observations in the CTZ [*Chavez et al.*, 1991]. The highest phytoplankton concentrations in the filament occur along the axis, where the velocities are lowest. On the northern and southern sides of the filament, where velocities are the highest, a sharp gradient in phytoplankton concentration exists. This gradient is stronger on the southern side of the filament.

The large-scale patterns in euphotic zone depth are similar to those simulated on day 140. The primary difference is the sharpening of the gradient in the euphotic zone at the edges of the filament. In these regions, the euphotic zone depth shallows from 180 m outside the filament to 40 m inside the filament over a distance of 35 km. Similar to the phytoplankton fields, the gradient in the euphotic zone depth is asymmetric, being stronger on the southern side of the feature.

After another 10 days (Plate 2c), the large-scale structure in the distribution of the phytoplankton still follows that of the circulation field. However, the magnitude of the phytoplankton concentration is reduced by about 50% relative to the initial concentrations. Phytoplankton mortality and zooplankton grazing are the dominant processes responsible for this decrease in phytoplankton biomass. The primary change by day 160 is that the asymmetry in euphotic zone decreases and the filament has become more pronounced. On the northern side of the filament, the euphotic zone depth shallows from 180 m to 60 m in a distance of 80 km, while on the southern side it shallows from 180 m to 60 m in 30 km.

The vertical distribution of the subsurface PAR field at these alongshore locations (Figure 3) shows that the penetration of a given isolume is quite variable moving onshore to offshore in the filament. Decreased light penetration, and hence a shallower euphotic zone, occurs within the filament due to the enhanced chlorophyll concentrations that develop in response to the nutrients upwelled along the edges of the filament. The magnitude of the upwelling is greater on the southern side of the filament (Plate 1); hence the stronger gradient in euphotic zone depth.

3.3. Across-Shore Carbon Distribution and Flux

It has been suggested that the filaments extending offshore in the CTZ provide a mechanism for transporting carbon and nitrogen from coastal regions to the oligotrophic offshore waters [*Strub et al.*, 1991; *Jones et al.*, 1991]. To test this hypothesis, the simulated biological distributions were converted from nitrogen to carbon using a C:N ratio of 6 and summed. These values, when multiplied by the across-shore velocity component, provide an estimate of the total carbon flux. It should be noted that regions of high carbon flux can coincide with regions of high across-shore velocities and are not necessarily indicative of regions of high carbon concentrations. The resultant surface carbon flux distributions obtained in this manner are shown in Plates 3 and 4.

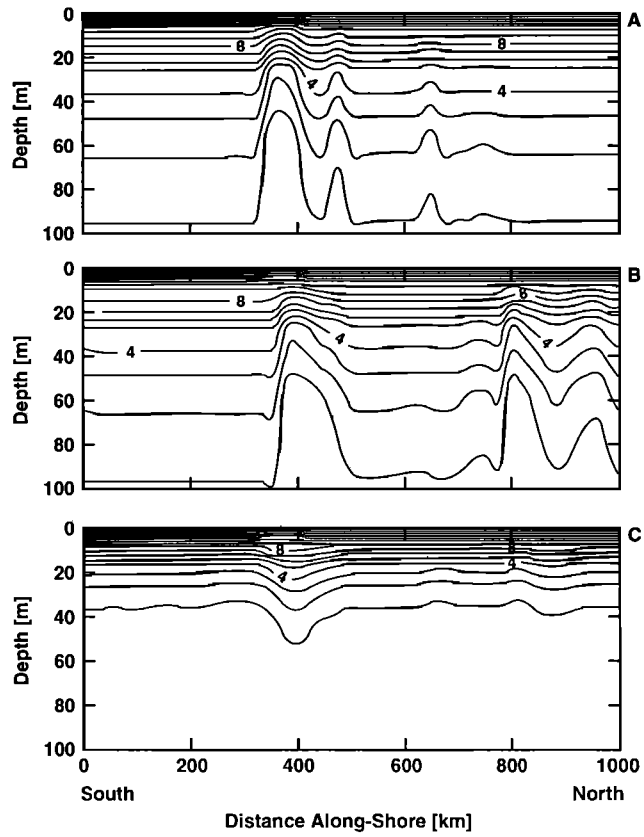

Figure 3. Simulated vertical distributions of the upper PAR field in the upper 100 m from model day 156 from along-shelf sections located (a) 77 km, (b) 280 km and (c) 511 km offshore. Contours intervals are 1 E m^{-2} s^{-1} x 10^{-4}. The actual positions of these sections are shown in Figure 2.

Initially, a region of offshore surface carbon flux that reaches values of greater than 21 mg C $m^{-2}s^{-1}$ occurs along the northern edge of the filament (Plate 3a). A smaller region of onshore flux occurs along the southern edge of the feature. Smaller regions of offshore and onshore surface carbon flux are distributed along the coastal and shelf break regions. These smaller-scale features are also seen in the circulation fields.

By model day 150 (Plate 3b), the regions of offshore and onshore carbon flux associated with the filament extend offshore to about 450 km. The offshore and onshore surface carbon fluxes are essentially equal, with maximum values of about 21 mg C $m^{-2}s^{-1}$. By day 160 (Plate 3c), the across-shore surface carbon flux is reduced because of the overall reduction in phytoplankton and zooplankton concentrations. The largest offshore and onshore fluxes are still associated with the high across-shore horizontal velocities associated with the filament (Plate 4) and are still somewhat symmetric. This pattern implies that there is a little to no net across-shore transport of surface carbon associated with the filament.

To further investigate carbon transport in the CTZ, the depth-integrated (to 1% PAR) carbon flux was cal-

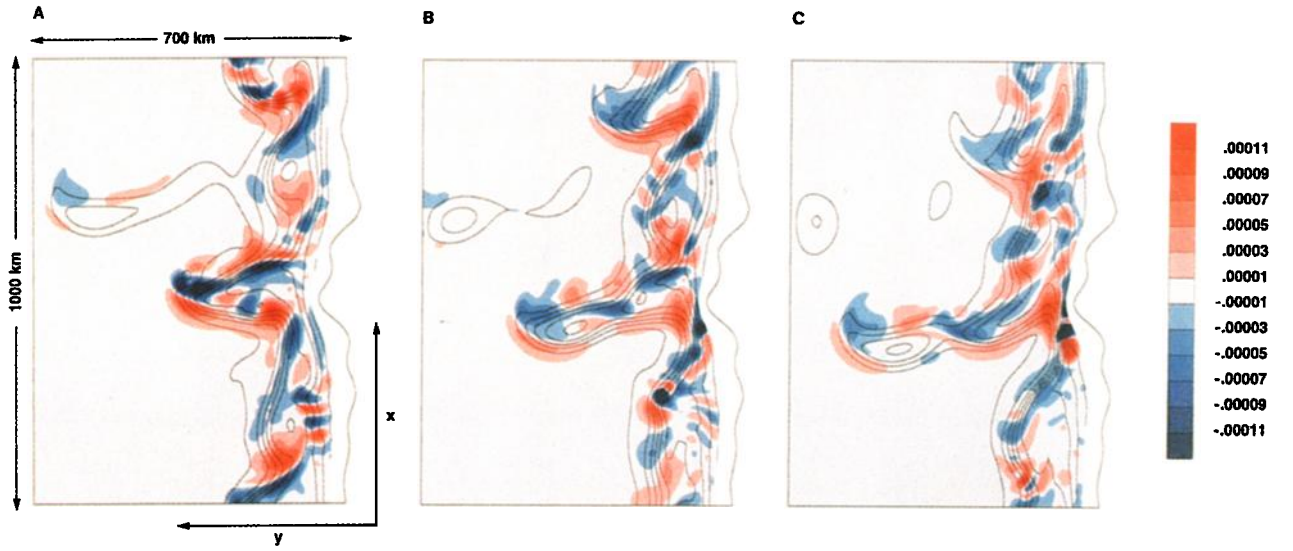

Plate 1. Horizontal distribution of vertical velocity (color; m s^{-1}) and density (line contours; σ_t) at 100 m depth from days (a) 140, (b) 150, and (c) 160 of the circulation simulation. Line contours for density range from 23.6 to 25.4 by intervals of 0.2. Upwelling and downwelling velocities with magnitudes greater than 11 x 10^{-5} m s^{-1} are shown in dark red and dark blue, respectively. Details of the CTZ circulation model are given by *Haidvogel et al.* [1991b].

culated (Plate 5). When presented in this fashion, pronounced regions of asymmetry appear in the onshore and offshore carbon flux. In particular, the offshore carbon flux on the northern side of the filament is much greater than the onshore carbon flux to the south. As the simulated fields evolve over the next 20 days, this asymmetry in offshore and onshore carbon flux in the filament persists. However, the magnitude of the flux diminishes over time.

The depth-integrated carbon flux estimates (see Plate 5) indicate that there may be preferred regions in the model domain for onshore and offshore carbon flux. In order to determine this, the carbon flux as a function of distance offshore was obtained by integrating the simulated carbon distributions vertically down to the 1% PAR level [$h_{1\%\mathrm{PAR}}$] and along-shore as

$$\mathrm{flux}(y) = \int_0^{-h_{1\%\mathrm{PAR}}} \int_0^{1000\mathrm{km}} (vC)\,dA, \qquad (8)$$

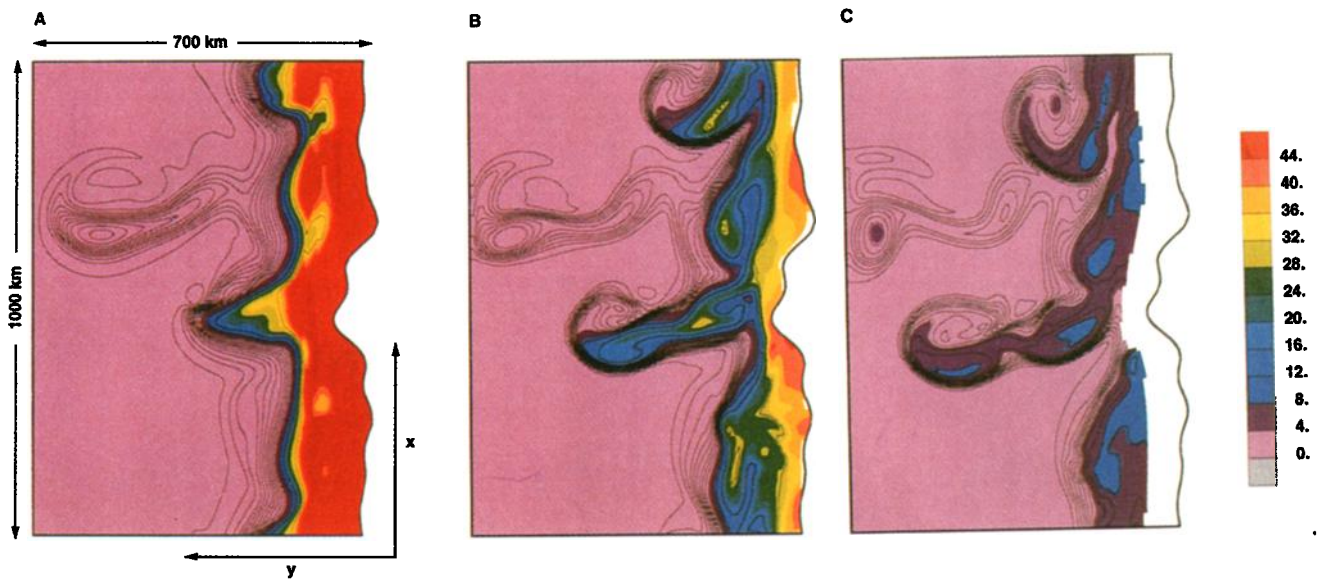

Plate 2. Horizontal distributions of the phytoplankton (LPP + SPP) field integrated over the depth of the euphotic zone (color; mg N m^{-3}) and euphotic zone depth, (line contours; meters) for days (a) 140, (b) 150, and (c) 160 from the 3-D physical-bio-optical model. Line contours for euphotic zone depth range from 30 to 180 m, 40 to 180 m, and 60 to 180 m in Plates 2a, 2b, and 2c, respectively, by intervals of 10. The euphotic zone depth is defined as the depth at which PAR is 1% of that calculated at the surface.

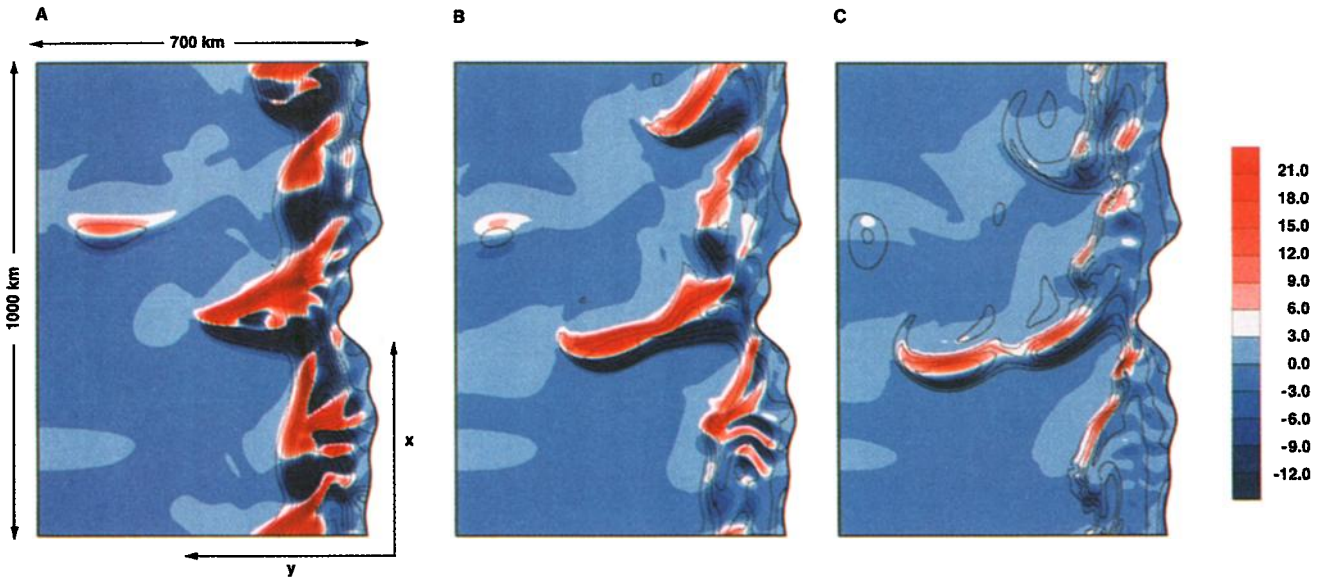

Plate 3. Horizontal distributions of the surface phytoplankton (LPP + SPP) carbon flux field (color; mg C m^{-2} s^{-1}) and surface phytoplankton (LPP + SPP) carbon field (line contours; mg C m^{-3}) for days (a) 140, (b) 150, and (c) 160 from the 3-D physical-bio-optical model. Line contours for surface phytoplankton carbon range from 25 to 400 mg C m^{-3} by intervals of 25, 25 to 175 mg C m^{-3} by intervals of 25, and 10 to 70 mg C m^{-3} by intervals of 10 in Plates 3a 3b, and 3c, respectively. Red colors indicate regions of offshore carbon flux. Dark blue colors indicate regions of onshore carbon flux.

where flux(y) is the across-shore carbon flux, v is the across-shore advective velocity and C is the sum of the carbon concentrations for all the biological constituents, including detritus. The resulting across-shore carbon transports calculated from the simulated distributions at days 140, 150, and 160 are shown in Figure 4.

On day 140, the maximum offshore and onshore carbon flux (Figure 4a) were 5600 and 4000 kg C s^{-1}, respectively. The maximum in both was located about 150 km offshore, with the onshore maximum being slightly inshore of the offshore maximum. The net across-shore carbon flux (Figure 4b) was 2200 kg C s^{-1}

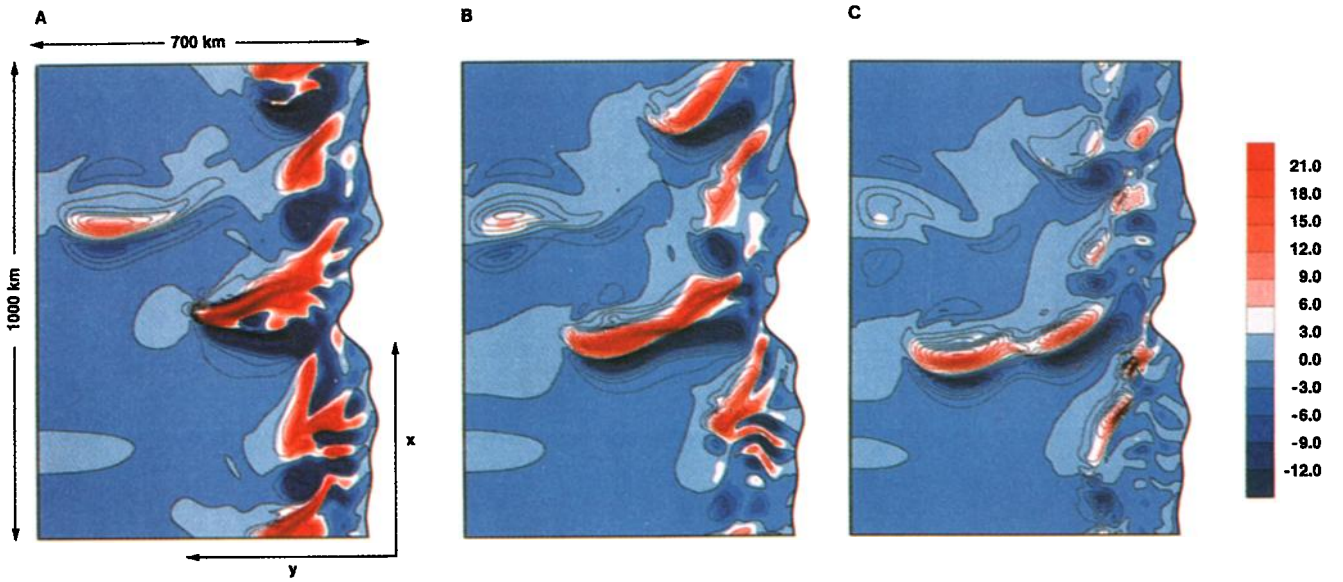

Plate 4. Horizontal distributions of the surface phytoplankton (LPP + SPP) carbon flux field (color; mg C m^{-2} s^{-1}) and surface across-shore velocity field (line contours; m s^{-1}) for days (a) 140, (b) 150, and (c) 160 from the 3-D physical-bio-optical model. Line contours for surface across-shore velocity field range from -0.8 to 0.9 m s^{-1}, -0.7 to 0.9 m s^{-1}, and -0.6 to 1 m s^{-1} in Plates 4a, 4b, and 4c, respectively, by intervals of 0.1. Red colors indicate regions of offshore carbon flux. Dark blue colors indicate regions of onshore carbon flux.

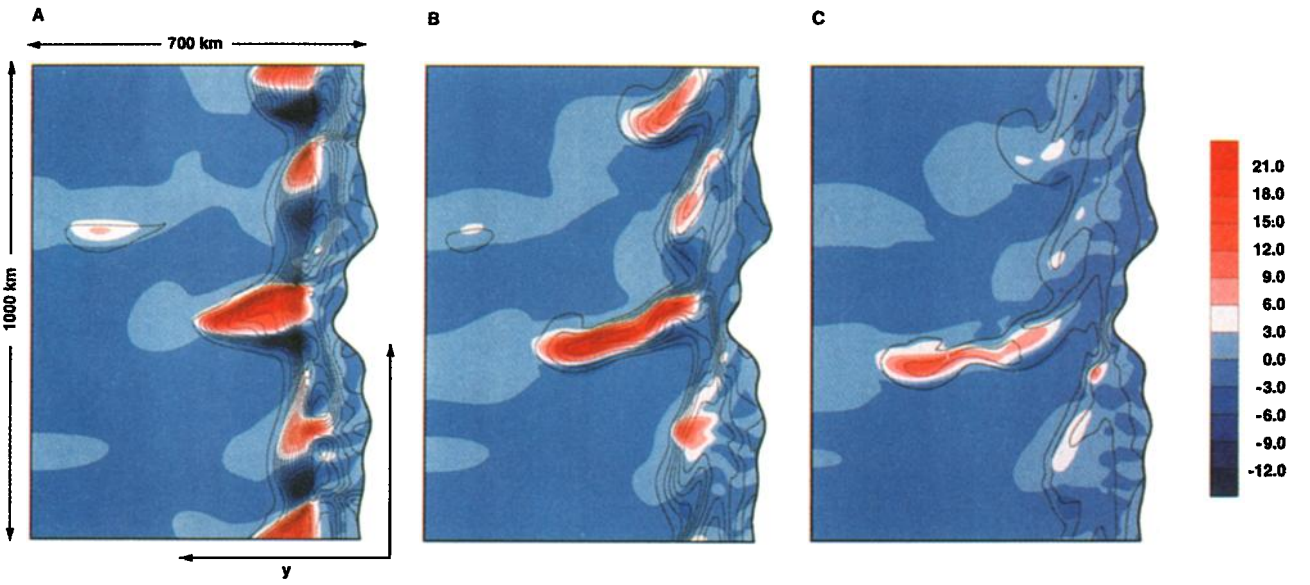

Plate 5. The horizontal distributions of the depth-integrated (to 1% PAR) total carbon (phytoplankton + zooplankton + detritus) flux field (color; g C m^{-1} s^{-1}) and depth-integrated carbon field (line contours; mg C m^{-2}) for days (a) 140, (b) 150, and (c) 160 from the 3-D physical-bio-optical model. Line contours for depth integrated carbon fields range from 25 to 425 mg C m^{-2}, 25 to 250 mg C m^{-2}, and 25 to 100 mg C m^{-2} in Plates 5a, 5b, and 5c, respectively, by intervals of 25. Red colors indicate regions of offshore carbon flux. Dark blue colors indicate regions of onshore carbon flux.

offshore and was centered about 200 km offshore. Over the next 20 days of integration the magnitude of the onshore and offshore carbon fluxes diminished and the peak of the maximum flux shifted offshore. The net transport continued to be offshore at the end of the simulation (day 160), the maximum offshore transport was 500 kg C s^{-1} and was located about 500 km from the coast.

The net across-shore carbon flux, flux(y), can be further integrated over the time of the simulation to obtain a total across-shore carbon flux,

$$\text{tflux(y)} = \int_0^{20\text{days}} \text{flux(y)dt}. \qquad (9)$$

The results of this calculation (Figure 5) show that no onshore transport of carbon occurred during the 20 day simulation. Offshore carbon transport occurred at several locations offshore, with the largest peak (35 x 10^9 g C) being about 500 km offshore. Smaller offshore transports occur at 100 and 300 km offshore.

4. Discussion and Conclusions

4.1. Three-Dimensional Circulation Fields

The simulated circulation patterns used for the 20-day integration of the biological quantities include the development of a distinct offshore propagating filament (Plate 1). The processes and dynamical balances underlying the formation of this filament have been previously discussed by *Haidvogel et al.* [1991a]. However, it is appropriate to mention the aspects of the simulated circulation fields that are relevant to the development of the patterns observed in the simulated biological fields.

The circulation fields show several distinct features that occur at a variety of time and length scales. By model day 140, a meander developed near the coastal bump, and over the course of the 20-day simulation this meander propagated offshore to form a filament. By model day 160, an eddy dipole had formed at the offshore tip of the filament, which is consistent with observed circulation features in the CTZ. The characteristic length scales and velocities for the simulated filament are fairly representative of those observed within the CTZ. The filament was advected offshore approximately 500 km and the width of the filament was about 75 km [*Haidvogel et al.*, 1991a], which compare well to the the CTZ field data. The filaments observed within the CTZ typically extend offshore more than 300 km [*Flament et al.*, 1985] and have widths of approximately 75 km [*Strub et al.*, 1991]. Maximum horizontal velocities within the simulated filament (0.8 to 1 m s^{-1}) were similar to those observed in the CTZ field data, 0.8 m s^{-1} [*Kosro and Huyer*, 1986; *Brink and Cowles*, 1991; *Strub et al.*, 1991]. The offshore flowing regions associated with the filament observed in the CTZ have been associated with large downwelling velocities of up to 10–40 m d^{-1} [*Kadko et al.*, 1991; *Dewey et al.*, 1991]. Maximum downwelling velocities of approximately 12 m d^{-1} were observed in the simulated circulation field. As in the field observations, these downwelling regions were also located in the northern offshore flowing region of the simulated filament.

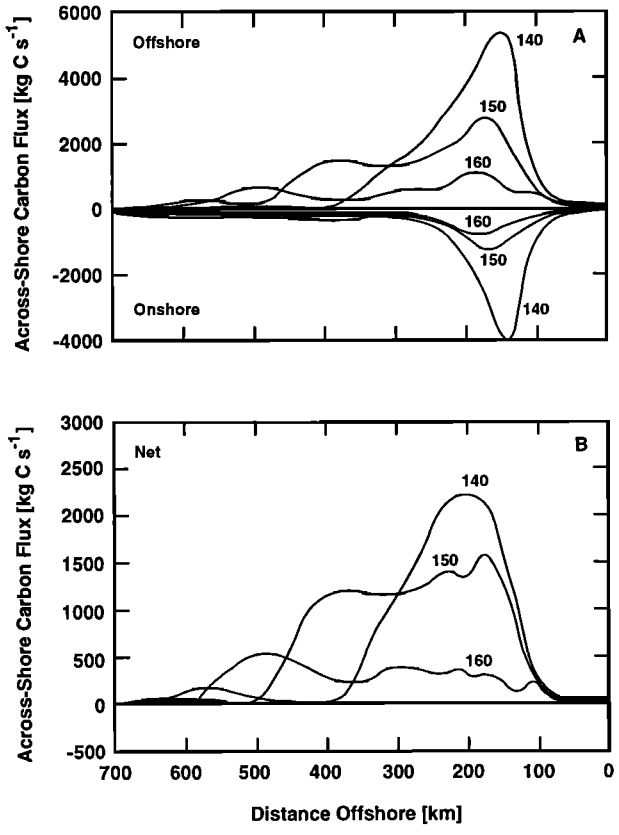

Figure 4. (a) Area-integrated across-shelf carbon flux calculated from the simulated biological distributions on days 140, 150, and 160. (b) Net across-shelf carbon flux for model days 140, 150, and 160. Positive values indicate offshore carbon flux; negative values are onshore flux.

Other circulation patterns were observed within the simulated circulation pattern which play a role in the development of the resulting biological and optical distributions. Mesoscale meanders propagates along the shelf, deforming the developing density field as they propagated south. Along these density fronts, frontal instabilities developed [*Haidvogel et al.*, 1991a] which moved south along the density front. Onshore of this density front, a series of wave-like downwelling and upwelling regions propagated to the north which was evidence for coastally trapped waves. While the filament was the dominant circulation feature affecting the development of the biological fields, these smaller-scale circulation patterns also played a role. The effect of these smaller-scale features on the across-shore flux and transport of carbon will be discussed.

Finally, the physical model was able to reproduce qualitatively other features within the CTZ such as the California Current and the California Countercurrent [*Haidvogel et al.*, 1991a]. However, except for the filament region, most of the variability of the simulated biological fields was in vertical and across the shore directions. The alongshore circulation had less of a role in structuring these distributions. Therefore the discussion of the resulting bio-optical fields, which follows in the next section, is focused on across-shore and within-filament variations.

4.2. Three-Dimensional Bio-Optical Fields

The results from the model showed that as the filament began to form, nutrient-rich water was upwelled into the upper water column, where it was removed by phytoplankton. This is consistent with the CTZ field observations, where over the initial 3–5 days of filament formation, the diatom community underwent a period of rapid growth in the core of a filament [*Hood et al.*, 1990, 1991; *Chavez et al.*, 1991]. As the simulated filament matured, nutrients were depleted, and the phytoplankton population diminished as a result of nutrient limitation and increased grazing pressure. Thus the simulated filaments also served as a stimulus for secondary production by providing conditions favorable for zooplankton growth and reproduction as these populations were advected offshore. These results are in agreement with observations of elevated zooplankton concentrations in the offshore regions of the CCS [*Chelton et al.*, 1982].

The general across-shore, model-derived phytoplankton distributions are similar to those observed within the CTZ. Phytoplankton concentrations are highest onshore (e.g. $>$ 1 mg chlorophyll a m^{-3}) and decreased rapidly (e.g. $<$ 0.1 mg chlorophyll a m^{-3}) across the

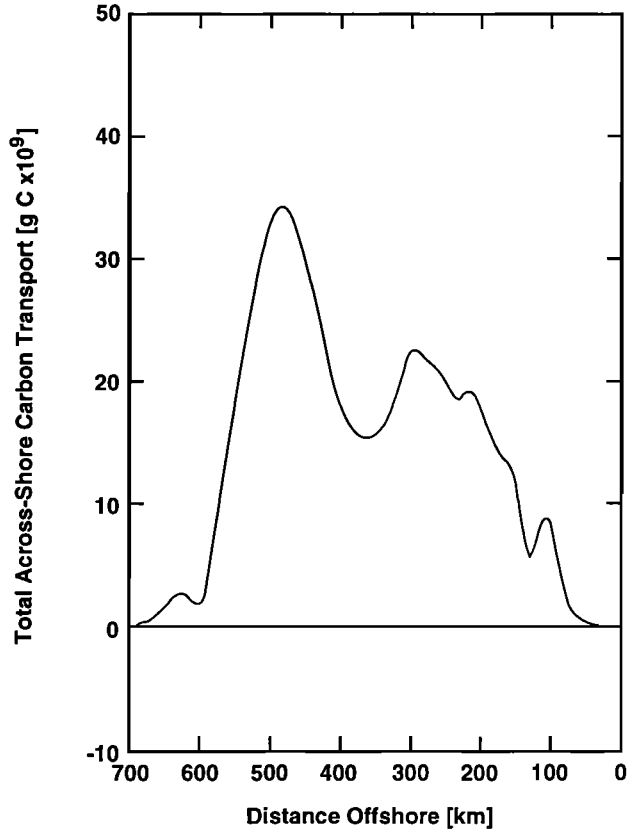

Figure 5. Total across-shore carbon transport after 20 days of simulation. Positive values indicate offshore across-shelf transport.

density front [*Hood et al.*, 1990, 1991; *Chavez et al.*, 1991].

A rapid decrease in the simulated phytoplankton field was observed to occur in both the filament and coastal regions. This rapid decrease in phytoplankton population within the filament was also observed in the CTZ region. An example of this rapid change was observed during the CTZ 1988 field surveys. *Chavez et al.* [1991] noted that the phytoplankton population decreased rapidly from a maximum of 9 mg chlorophyll *a* m^{-3} ($\approx$ 2500 cells mL^{-1}) to less than 0.5 mg chlorophyll *a* m^{-3} [$<$ 100 cells mL^{-1}] in a period of about 24 days. Also, *MacIsaac et al.* [1985] noted that the timescale of nutrient depletion in coastal upwelling systems is of the order of 5–10 days. While our results from the filament region compare well to the CTZ observations, the decrease in phytoplankton along the coast suggests that we may need to alter or better parameterize several of the model processes in order to better simulate the coastal regions of the CTZ. However, given the large initial concentration of zooplankton along the coast, it may also be that the large decrease along the coast is indeed due to the initial zooplankton concentrations. The decrease along the coast may also not be related to the filament but could be caused by lack of appropriate coastal circulation or mixing and/or coastal remineralization processes. However, because the phytoplankton biomass concentrations within the filament compare well to the observations in concentration, distribution and timescales, we feel confident that the model and therefore the carbon flux and transport estimates are valid for the filament region. Finally, the results from the 1-D model [*Moisan and Hofmann*, this issue(a)] showed that the transient response or adjustment due to the initial conditions had a timescale of less than 5 days for the phytoplankton and nutrient fields.

Simulated phytoplankton concentrations were highest in the core of the filament (e.g., $>$ 2.5 mg chlorophyll *a* m^{-3}) and decreased across the filament's density front (e.g., $<$ 0.5 mg chlorophyll *a* m^{-3}) on the outer edges of the filament. The distance over which this change took place was shorter (30 km) in the onshore flowing, southern flank of the filament, where high upwelling velocities concentrated the phytoplankton near the surface. In the northern, offshore-flowing flank of the filament, high downwelling velocities and substantial across-jet exchange [*Hofmann et al.*, 1991] caused this change to occur over a longer distance (80 km).

Due to the paucity of data on the spatial distribution of the subsurface light field within in the CTZ, comparison of the simulated light fields with observations is very limited. The general across-shelf variations in the depth of the simulated euphotic zone depth ranged from approximately 30 m onshore to approximately 180 m offshore, with the largest change in euphotic zone depths occurring in the region of the density fronts. The available 1% PAR measurements from the CTZ [*Moisan and Hofmann*, this issue(a)] show a similar trend, with the shallowest 1% PAR level being about 20 m onshore and deepening to a maximum ($>$ 130 m) offshore. Shallow 1% PAR levels ($\approx$ 30 m) were also observed within the filaments during the CTZ field surveys [*Washburn et al.*, 1991].

As in the simulated phytoplankton fields, the across-filament variation in the depth of the euphotic zone is asymmetric. The euphotic zone shallows more rapidly on the southern, onshore flowing portion of the simulated filament and mesoscale meanders and eddies. The available light measurements from the CTZ do not have sufficient spatial resolution to provide a detailed comparison to the simulated feature. However, because such asymmetry is observed in the across-filament CTZ phytoplankton fields [*Jones et al.*, 1991], such a feature should exist due to attenuation of light by the phytoplankton populations.

The euphotic zone depth is the result of the interaction of several biological processes. As an example, grazing removed the nutrient-limited, slow growing phytoplankton from the upper regions in the water column, which then let light penetrate further into the water column. This increase in light penetration allowed enhanced phytoplankton growth at depth. Thus the net effect of zooplankton grazing was to increase the total integrated primary production within the water column. The interplay of these processes in affecting euphotic zone depth is discussed in the sensitivity analysis of the one-dimensional model presented by *Moisan and Hofmann* [this issue(a)].

4.3. Across-Shore Carbon Flux and Transport

The across-shore flux of carbon from highly productive coastal regions may be an important carbon pathway in the ocean biogeochemical carbon cycle [*Jahnke*, 1990]. However, little is known about the relative contribution of carbon export from coastal regions to the open ocean to the overall global carbon cycle. The magnitude of carbon flow through this pathway needs to be known to better understand the fate and ultimate effect of natural and anthropogenic carbon inputs on the ocean.

As the filament developed in the simulated circulation fields, it moved offshore about 300 km in 20 days. Using these values, the rate of filament elongation is about 17 cm s^{-1}. This is about one-third the velocities observed in the fast moving density front regions in the filament (see Plate 1). The circulation field of the filaments both advects water around the density front and elongates the filament, thus propagating it offshore. The following discussion will demonstrate the importance of each of these distinct components of the velocity field in the cross-shore flux and transport of carbon.

The simulated surface carbon flux fields (see Plates 3 and 4) suggest that there are specific regions within the filament which are responsible for the majority of the across-shore flux of carbon. The highest offshore surface carbon flux (e.g., $>$ 21 mg C m^{-2} s^{-1}) occurred along the northern flank of the filament, coincident with the region of highest offshore velocities. Likewise, the highest onshore surface carbon flux (e.g., $>$ 12 mg C m^{-2} s^{-1}) occurred along the southern flank of the filament in the region of highest onshore velocities. The

velocities in the density front region simply advected water offshore in the northern portion of the filament and then back onshore in the southern portion of the filament. The velocities were larger in the offshore than in the onshore flowing portion because the filament was elongating. Along the core of the filament, where phytoplankton concentrations are highest, the across-shore flux of carbon is lowest because of the low across-shore velocities, coincident with the high carbon concentrations. In this region, the velocities were primarily those associated with the filament's elongation. The addition of an elongation velocity to the onshore and offshore velocities associated with water flowing along the filament has several effects on the onshore and offshore velocities. All offshore velocities increased in magnitude. All onshore velocities with magnitudes greater than the elongation velocities decreased in magnitude. Also, all onshore velocities with magnitudes lower than the elongation velocities changed to an offshore velocity. The net effect of the filament elongation was to increase (decrease) the aerial extent of the offshore (onshore) surface carbon flux field regions.

Estimates of surface across-shore flux of carbon have not been made from measurements from the CTZ. However, both the simulated surface horizontal velocity and phytoplankton fields, which were used to calculate the surface across-shore carbon flux fields, resemble those measured within the CTZ [*Flament et al.*, 1985; *Hayward and Mantyla*, 1990; *Hood et al.*, 1990, 1991; *Hood*, 1990; *Huyer et al.*, 1991; *Washburn et al.*, 1991; *Jones et al.*, 1991; *Strub et al.*, 1991]. The near-surface chlorophyll and nitrate concentrations and temperature fields obtained in July 1986 for a region offshore Point Arena during a filament event can be used to verify the model-derived distributions. Water temperatures were lower than 12°C along the coast and within the core of the filament which was observed to extend seaward near Point Arena. High chlorophyll (> 5 mg m^{-3}) and nitrate (> 10 mg m^{-3}) concentrations were coincident with these regions of colder temperatures [*Jones et al.*, 1991]. Satellite-derived estimates of sea surface temperature and pigment concentrations [*Brink and Cowles*, 1991] show similar patterns. Other field studies which measured the pigment concentrations within the CTZ region [*Hood et al.*, 1990, 1991; *Chavez et al.*, 1991] also found high chlorophyll coincident with cold temperatures.

All CTZ field surveys measured a strong seaward flow north of the observed temperature minimum in the filament with maximum velocities of approximately 0.8 m s^{-1} [*Huyer et al.*, 1991]. Velocities were minimal within the pigment core of the filament, and slower onshore velocities were observed on the southern flank [*Rienecker and Mooers*, 1989; *Huyer et al.*, 1991, *Chavez et al.*, 1991; *Jones et al.*, 1991]. As in the simulation, these results suggest a developing circulation feature composed of a velocity field which advects water along constant density contours and also elongates the feature. The resulting lower onshore velocities on the southern flank of the observed filaments suggest the offshore propagation and elongation of the observed circulation patterns.

From the filaments and surface nutrient concentrations observed in the CTZ field surveys, *Chavez et al.* [1991, p. 14,840] concluded that "the strong baroclinic jets commonly found in the coastal transition zone ... are not responsible for significant transport of coastally upwelled, high-nutrient water to the ocean interior." Their conclusion was based on the observation that the regions of highest nutrients and phytoplankton biomass were not associated with the observed high offshore velocities. This was also observed in the model results. However, the values of the across-shore flux of carbon and nutrients are obtained by the product of the concentration of carbon or nutrients and the across-shore velocities. Therefore regions of high across-shore velocities can also be regions of high across-shore flux of carbon and nutrients, as observed in the simulated carbon flux distributions.

In addition to filament-related features, several other circulation features present in the simulated fields warrant discussion because of their role in the across-shore flux and transport of carbon. The mesoscale meanders and eddies were characterized by high phytoplankton concentrations, especially along the axis of the meanders. Also, high across-shore velocities were observed to be associated with the density fronts of the meanders and eddies. The resulting patterns in the across-shore surface carbon flux of these meanders and eddies resembles that observed in the filament.

The presence of the frontal instabilities [*Haidvogel et al.*, 1991a] and phenomena resembling coastally trapped waves introduced even smaller-scale variability in the simulated circulation and biological fields. Such wave-like features were observed in the AVHRR [*Rienecker and Mooers*, 1989] and CZCS [*Peláez and McGowan*, 1986] imagery of the filaments in the CTZ. The effect of these small-scale features on the across-shore flux of carbon may be important. Because the frontal instabilities are superimposed upon the mesoscale meanders and eddies, their contribution to the across-shore carbon flux is difficult to quantify in the simulated across-shore carbon flux fields. However, the contribution of the phenomenon resembling coastally trapped waves to the surface across-shore flux of carbon was clearly observable, since it was located onshore of the density front (see Plate 1). Small-scale wave-like regions off onshore and offshore velocities create similar small-scale wave-like patterns in the surface across-shore carbon flux (see Plate 4).

The depth-integrated total across-shore carbon flux fields calculated from the simulated fields (see Plate 5) show a different pattern than that observed in the surface across-shore flux fields (see Plate 4). The depth-integrated (integrated to 1% PAR) across-shore carbon flux is primarily offshore because the net volume flux of the filament is offshore due to the elongation of the feature. Filament elongation causes a net surface offshore volume flux. Such a net surface offshore volume flux within the filament was observed in the CTZ by *Jones et al.* [1991]. In their study they observed a 0.80-Sv volume flux in the offshore direction and 0.72-Sv flux in the onshore direction within the top 100 m of a fila-

ment. This resulted in a net offshore volume flux of 0.08 Sv. However, it is difficult to directly compare these field results with the model results given the temporal and spatial dependence of these simulated and observed fields.

The time series of the area-integrated across-shore carbon flux demonstrates how variable the carbon flux estimates are in time and distance from shore (see Figure 4). The difference between the offshore and onshore flux estimates (see Figure 4a) gives the net across-shore flux at any distance offshore (see Figure 4b). The area-integrated values of the net across-shore carbon flux essentially remove the effect of the velocity components associated with the meandering density front from those responsible for the filament's offshore propagation. On model day 140, there is a maximum in the net across-shore carbon flux at about 200 km from the coast. By model day 150, the elongation of the filament had modified the form of the net across-shore carbon flux. While a maximum is still observed at approximately 200 km offshore, across-shore flux values are higher than 1000 kg C s^{-1} between approximately 150 and 450 km offshore. The eddy dipoles which were observed to form at the offshore end of the filament are responsible for the offshore maximum in the across-shore flux at approximately 500 km on model day 160.

The resulting time-integrated total across-shore carbon transport for the 20 days over which the model was integrated is everywhere offshore (see Figure 5). The highest across-shore transport of carbon is approximately 35 x 10^9 g C and occurs approximately 500 km from shore. Most of this transport is composed of phytoplankton biomass. If a constant carbon to chlorophyll ratio of 40 (mg C:mg chlorophyll *a*) is assumed, the maximum carbon transport converts to a chlorophyll transport of approximately 506 g chlorophyll *a* s^{-1}. *Jones et al.* [1991] obtained transport values of 280 g chlorophyll *a* s^{-1} by integrating a 110-km-wide filament cross section from 0 to 100 m. A higher estimate of 347 g chlorophyll *a* s^{-1} was obtained by *Strub et al.* [1991] by integrating a 200-km-wide filament cross section from 0 to 100 m. Keeping in mind the highly variable nature of the filaments in time and space, the model-derived estimate of the across-shore transport agrees reasonably with that obtained from the CTZ field data.

An estimate of the total annual transport of carbon can be obtained from the above transport estimates. Filaments are generated within the CTZ from May to October for a total of about 3–6 months [*Strub et al.*, 1991] and have a lifetime of about one month. Also, as many as 1–6 filaments have been observed in various stages of development along the western coast of the United States [*Strub et al.*, 1991]. Using these estimates, the filaments along the California coast can transport between 158 and 1890 g C m^{-2} yr^{-1} as much as 500 km offshore. This large offshore transport of carbon may supply the high zooplankton biomass observed to exist approximately 200 km offshore in the southern region of the CTZ [*Chelton et al.*, 1982].

Numerous estimates of across-shore flux of carbon have been made for different regions (Table 3). The large differences that exist between these environments make comparisons difficult. For example, our estimate of the across-shore carbon transport in the CTZ is higher than that estimated off the coast of Peru, although both are upwelling systems. One factor which may help to explain this difference is that the Peruvian upwelling system does not produce filament-like structures; upwelling off the Peruvian coast never extends off the shelf [*Brink et al.*, 1983]. However, even with these observed differences, the CTZ is potentially an important site for across-shore carbon transport.

The results from coupling a bio-optical food web model to a 3-D circulation model which was designed to simulate the circulation features observed within the CTZ support the following conclusions.

1. The center of the filaments advect nutrient-rich coastal waters offshore several hundred kilometers.

2. The product of the horizontal velocities and carbon concentrations indicate that the regions of highest onshore and offshore carbon flux are not regions of high carbon concentration but rather are regions of high cross-shore velocities.

3. The high offshore and onshore velocity regions are not responsible for the net flux of carbon offshore. Rather, the highest net offshore carbon flux region is associated with the center of the filament.

Table 3. Estimates of Across-Shore Carbon Flux Obtained for a Variety of Environments

Region	Carbon Flux, g C m^{-2} yr^{-1}	Reference
Texas–Louisiana shelf	56[a]	*Walsh* [1988]
Southeastern Bering Sea	79	*Walsh* [1988]
New York shelf	180[a]	*Walsh* [1988]
Anadyr Water, Bering Sea	118[a]	*Walsh* [1988]
Georges Bank	240	*Walsh* [1988]
Peru (≈1966–1969)[b]	82[a]	*Walsh* [1988]
Peru (≈1976–1979)[c]	591[a]	*Walsh* [1988]
CTZ	158–1890	this study

[a] Includes burial
[b] Before overfishing of anchovy population
[c] After overfishing of anchovy population

4. The time rate of change of the food web within the filament is consistent with that observed within the CTZ. Newly upwelled water supports a phytoplankton bloom which over a 5-day period quickly draws down the nutrient load as it is advected offshore within the core of the filament. The bloom, thereafter, rapidly decays over the next 10 days as a result of decreased nutrient supply and zooplankton grazing.

5. Using observations from the CTZ, the annual integrated carbon transport by filaments along the California coast is estimated to be 1.89 x 10^{12} g C. This large offshore transport of carbon may supply the high zooplankton biomass observed to exist approximately 200 km offshore in the southern region of the CTZ [*Chelton et al.*, 1982].

6. Other physical processes such as coastally-trapped waves and frontal instabilities may also be important in cross-shore carbon transport.

Acknowledgments. Special thanks go to K. S. Hedström for helping us understand and use the SPEM code. We thank R. Bidigare, R. Hood, S. Smith, D. Mackas, L. Washburn, B. Jones, C. Davis, F. Chavez, J. Huyer, C. Paulson and others within the CTZ group for providing us with the wealth of data used to complete this study. This research was supported by the Office of Naval Research under grant N00014-90-J-1930. Computer resources and facilities were provided by the Commonwealth Center for Coastal Physical Oceanography, Naval Research Laboratory, and Stennis Space Center. This support is gratefully acknowledged. This research was performed by J.R.M. in partial fulfillment of the requirements for a Ph.D. degree at Old Dominion University.

References

Abbott, M. R., and B. Barksdale, Phytoplankton pigment patterns and wind forcing off central California, *J. Geophys. Res.*, *96*, 14,649-14,667, 1991.

Abbott, M. R., and P. M. Zion, Satellite observations of phytoplankton variability during an upwelling event, *Cont. Shelf. Res.*, *4*, 661-680, 1985.

Abbott, M. R., and P. M. Zion, Spatial and temporal variability of phytoplankton pigment off northern California during Coastal Ocean Dynamics Experiment 1, *J. Geophys. Res.*, *92*, 1745-1756, 1987.

Atkinson, L. P., K. H. Brink, R. E. Davis, B. H. Jones, T. Paluszkiewicz, and D. W. Stuart, Mesoscale variability in the vicinity of points Conception and Arguello during April-May 1983: The OPUS 1983 Experiment, *J. Geophys. Res.*, *91*, 12,899-12,918, 1986.

Bernstein, R. L., L. Breaker, and R. Whritner, California Current eddy formation: Ship, air, and satellite results, *Science*, *195*, 353-359, 1977.

Bienfang, P., and J. Szyper, Effects of temperature and salinity on sinking rates of the centric diatom *Ditylum brightwelli*, *Biol. Oceanogr.*, *1*, 211-223, 1982.

Breaker, L. C., and R. P. Gilliland, A satellite sequence on upwelling along the California coast, in *Coastal Upwelling, Coastal Estuarine Sci.*, vol. 1, edited by F. A. Richards, pp. 87-94, AGU, Washington, D.C., 1981.

Brink, K. H., and T. J. Cowles, The Coastal Transition Zone program, *J. Geophys. Res.*, *96*, 14,637-14,647, 1991.

Brink, K. H., D. Halpern, A. Huyer, and R. L. Smith, The physical environment of the Peruvian upwelling system, *Prog. Oceanogr.*, *12*, 285-305, 1983.

Chavez, F., R. T. Barber, A. Huyer, P. M. Kosro, S. Ramp, T. Stanton and B. Rojas de Mendiola, Horizontal transport of nutrients in the coastal transition zone off northern California: Effects on primary production, phytoplankton biomass, and species composition, *J. Geophys. Res.*, *96*, 14,809-14,831, 1991.

Chelton, D.B., Seasonal variability of alongshore geostrophic velocity off central California, *J. Geophys. Res.*, *89*, 3473-3486, 1984.

Chelton, D. B., P. A. Bernal, and J. A. McGowan, Large-scale interannual physical and biological interaction in the California Current, *J. Marine Res.*, *40*, 1095-1125, 1982.

Chelton, D. B., A. W. Bratkovich, R. L. Bernstein, and P. M. Kosro, Poleward flow off central California during the spring and summer of 1981 and 1984, *J. Geophys. Res.*, *93*, 10,604-10,620, 1988.

Coastal Transition Zone Group, The Coastal Transition Zone program, *Eos Trans. AGU*, *69*(27), 698-699, 1988.

Dewey, R. K., J. N. Moum, C. A. Paulson, D. R. Caldwell, and S. D. Pierce, Structure and dynamics of a coastal filament, *J. Geophys. Res.*, *96*, 14,885-14,907, 1991.

Flament, P., L. Armi, and L. Washburn, The evolving structure of an upwelling filament, *J. Geophys. Res.*, *90*, 11,765-11,778, 1985.

Haidvogel, D. B., A. Beckmann, and K. S. Hedström, Dynamical simulations of filament formation and evolution in the coastal transition zone, *J. Geophys. Res.*, *96*, 15,017-15,040, 1991a.

Haidvogel, D. B., J. Wilkin, and R. E. Young, A semi-spectral primitive equation ocean circulation model using vertical sigma and orthogonal curvilinear coordinates, *J. Comput. Phys.*, *94*, 151-185, 1991b.

Hayward, T. L., and A. Mantyla, Physical, chemical and biological structure of a coastal eddy near Cape Mendocino, *J. Marine Res.*, *48*, 825-850, 1990.

Hedström, K. S., User's manual for a semi-spectral primitive equation regional ocean-circulation model, version 3.0, Tech. Note FY90-2, 82 pp., Inst. of Nav. Ocean., Stennis Space Cent., Miss., 1990.

Hofmann, E. E., K. S. Hedström, J. R. Moisan, D. B. Haidvogel, and D. L. Mackas, The use of simulated drifter tracks to investigate general transport patterns and residence times in the coastal transition zone, *J. Geophys. Res.*, *96*, 15,041-15,052, 1991.

Hood, R. R., Phytoplankton biomass, photosynthetic light response, and physical structure in a northern California upwelling system, Ph.D. thesis, 141 pp., Scripps Inst. of Oceanogr., La Jolla, Calif., 1990.

Hood, R. R., M. R. Abbott, A. Huyer, and P. M. Kosro, Surface patterns in temperature, flow, phytoplankton biomass, and species composition in the coastal transition zone off northern California, *J. Geophys. Res.*, *95*, 18,081-18,094, 1990.

Hood, R. R., M. R. Abbott, and A. Huyer, Phytoplankton and photosynthetic light response in the coastal transition zone off northern California in June 1987, *J. Geophys. Res.*, *96*, 14,769-14,780, 1991.

Huntley, M. E., M. Zhou, and W. Nordhausen, Mesoscale distribution of zooplankton in the California Current in late spring, observed by optical plankton counter, *J. Marine Res.*, *53*, 1-28, 1995.

Huyer, A. J., P. M. Kosro, J. Fleischbein, S. R. Ramp, T. Stanton, L. Washburn, F. P. Chavez, T. J. Cowles, S. D. Pierce, and R. L. Smith, Currents and water masses of the coastal transition zone off northern California, June to August 1988 *J. Geophys. Res.*, *96*, 14,809-14,831, 1991.

Jahnke, R. A., Ocean flux studies: A status report, *Rev. Geophys.*, *28*, 381-398, 1990.

Jones, B. H., C. N. K. Mooers, M. M. Rienecker, T. Stanton, and L. Washburn, Chemical and biological structure and

transport of a cool filament associated with a jet-eddy system off northern California in July 1986 (OPTOMA21), *J. Geophys. Res.*, *96*, 22,207-22,225, 1991.

Kadko, D. C., L. Washburn, and B. Jones, Evidence of subduction within cold filaments of the northern California coastal transition zone, *J. Geophys. Res.*, *96*, 14,909-14,926, 1991.

Kosro, P. M., and A. Huyer, CTD and velocity surveys of seaward jets off northern California, July 1981 and 1982, *J. Geophys. Res.*, *91*, 7680-7690, 1986.

Lentz, S. J., A description of the 1981 and 1982 spring transitions over the northern California shelf, *J. Geophys. Res.*, *92*, 1545-1567, 1987.

MacIsaac, J. J., R. C. Dugdale, R. T. Barber, D. Blasco, and T. T. Packard, Primary production cycle in an upwelling center, *Deep Sea Res.*, *32*, 503-529, 1985.

Mackas, D. L., L. Washburn, and S. Smith, Zooplankton community pattern associated with a California Current cold filament, *J. Geophys. Res.*, *96*, 14,781-14,797, 1991.

Magnell, B. A., N. A. Bray, C. D. Winant, C. L. Greengrove, J. Largier, J. F. Borchardt, R. L. Bernstein, and C. E. Dorman, Convergent shelf flow at Cape Mendocino, *Oceanography*, *3*, 4-11, 1990.

Michaelsen, J., X. Zhang, and R. C. Smith, Variability of pigment biomass in the California Current system, *J. Geophys. Res.*, *93*, 10,883-10,896, 1988.

Millero, F. J., and A. Poisson, International one-atmosphere equation of state of seawater, *Deep Sea Res.*, *28*, 625-629, 1981.

Moisan, J. R., and E. E. Hofmann, Modeling nutrient and plankton processes in the California coastal transition zone, 1, A time- and depth-dependent model, *J. Geophys. Res.*, this issue(a).

Moisan, J. R., and E. E. Hofmann, Modeling nutrient and plankton processes in the California coastal transition zone, 3, Lagrangian drifter experiments, *J. Geophys. Res.*, this issue(b).

Mooers, C. N. K., and A. R. Robinson, Turbulent jets and eddies in the California Current and inferred cross-shore transports, *Science*, *223*, 51-53, 1984.

Pelaéz, J., and J. A. McGowan, Phytoplankton pigment patterns in the California Current as determined by satellite, *Limnol. Oceanogr.*, *31*, 927-950, 1986.

Rienecker, M. M. and C. N. K. Mooers, Mesoscale eddies, jets, and fronts off Point Arena, California, July 1986, *J. Geophys. Res.*, *94*, 12,555-12,569, 1989.

Rienecker, M. M., C. N. K. Mooers, and A. R. Robinson, Dynamical interpolation and forecast of the evolution of mesoscale features off northern California, *J. Phys. Oceanogr.*, *17*, 1189-1213, 1987.

Simpson, J. J., and R. J. Lynn, A mesoscale eddy dipole in the offshore California Current, *J. Geophys. Res.*, *95*, 13,009-13,022, 1990.

Smayda, T. J., The suspension and sinking of phytoplankton in the sea, *Oceanogr. Mar. Biol.*, *8*, 353-414, 1970.

Smith, R. C., X. Zhang, and J. Michaelsen, Variability of pigment biomass in the California Current system as determined by satellite imagery, 1, Spatial variability, *J. Geophys. Res.*, *93*, 10,863-10,882, 1988.

Stramma, L., P. Cornillon, R. A. Weller, J. F. Price, and M. G. Briscoe, Large diurnal sea surface temperature variability: Satellite and in situ measurements, *J. Phys. Oceanogr.*, *16*, 827-837, 1986.

Strub, P. T., P. M. Kosro, A. Huyer, and the CTZ Collaborators, The nature of the cold filaments in the California Current system, *J. Geophys. Res.*, *96*, 14,743-14,768, 1991.

Thomas, A. C., and P. T. Strub, Interannual variability in phytoplankton pigment distributions during the spring transition along the west coast of North America, *J. Geophys. Res.*, *94*, 18,095-18,117, 1989.

Thomas, A. C., and P. T. Strub, Seasonal and interannual variability of pigment concentrations across a California Current frontal zone, *J. Geophys. Res.*, *95*, 13,023-13,042, 1990.

Thomson, R. E., and J. E. Papadakis, Upwelling filaments and motion of a satellite-tracked drifter along the west coast of North America, *J. Geophys. Res.*, *92*, 6445-6461, 1987.

Traganza, E. D., D. A. Nestor, and A. K. McDonald, Satellite observations of a nutrient upwelling off the coast of California, *J. Geophys. Res.*, *85*, 4104-4106, 1980.

Traganza, E. D., J. C. Conrad, and L. C. Breaker, Satellite observations of a cyclonic upwelling system and a giant plume in the California current, in *Coastal Upwelling, Coastal Estuarine Sci.*, vol. 1, edited by F. A. Richards, pp. 228-241, AGU, Washington, D.C., 1981.

Walsh, J. J., *On the Nature of Continental Shelves*, Academic, San Diego, Calif., 1988.

Washburn, L., D. C. Kadko, B. H. Jones, T. Hayward, P. M. Kosro, T. P. Stanton, S. Ramp, and T. Cowles, Water mass subduction and the transport of phytoplankton in a coastal upwelling system, *J. Geophys. Res.*, *96*, 14,927-14,945, 1991.

White, W. B., C. -K., Tai, and J. DiMento, Annual Rossby waves characteristics in the California Current region from the Geosat Exact Repeat Mission, *J. Phys. Oceanogr.*, *20*, 1297-1310, 1990.

D. B. Haidvogel, Institute of Marine and Coastal Sciences, Rutgers University, New Brunswick, NJ 08903.

E. E. Hofmann, Center for Coastal Physical Oceanography, Department of Oceanography, Old Dominion University, Norfolk, VA 23529.

J. R. Moisan, Physical Oceanography Research Division, Scripps Institution of Oceanography, La Jolla, CA 92093-0230. (e-mail moisan@vanilla.ucsd.edu)

(Received September 22, 1995; revised May 9, 1996; accepted May 23, 1996.)